From "stars" to nano: Porous poly(ethylene glycol) hydrogel films and nanosheets as a versatile platform for sensing and nanofabrication

Michael Zharnikov (✉)

Angewandte Physikalische Chemie, Universität Heidelberg, Im Neuenheimer Feld 253, D-69120 Heidelberg, Germany

ABSTRACT

The use of bioinert materials is crucially important for medicine and bioengineering. The most popular systems in this context are oligo- and poly(ethylene glycols) (OEGs and PEGs), applied generally in different forms as bulk materials, thin films, and functional molecular groups. Here, I review the fabrication, properties, and applications of porous hydrogel PEG films (PHFs) and nanosheets (PHNs) formed by thermally activated crosslinking of amino- and epoxy-terminated, star-branched PEG oligomers with variable molecular weight. These systems possess various useful characteristics, including tunable thickness and porosity, hydrogel properties, bioinertness, robustness, and extreme elasticity. They can serve as the basis for composite materials, advanced nanofabrication, and lithography, bioinert supports for high-resolution transmission electron microscopy, susceptible elements in micro-electromechanical systems, and basic building blocks of temperature, humidity, chemical, and biological sensors. Representative examples of the respective applications are provided. Even though these examples span a broad field-from nanoengineering to biosensing, the applications of the PHFs and PHNs are certainly not limited to these cases but can be specifically adapted and extended to other fields, such as tissue engineering and drug delivery, relying on versatility and tunability of these systems.

KEYWORDS

poly(ethylene glycol), hydrogel films, bioinertness, nanosheets, sensors, composite materials

1   Introduction

The use of reliable bioinert materials is crucially important for modern medicine, bioengineering, and biosensing. Various materials possessing these properties have been reported, including phosphocholine, polysaccharides, mannose, etc. The most popular and frequently used type of these materials is, however, poly(ethylene glycol) (PEG) [1–4]. PEG is a non-toxic, hydrophilic, synthetic polymer resisting nonspecific protein adsorption [1–3], and cell adhesion [5], including the activation of immune cells [6], which is the initial step of the inflammation reaction. Consequently, PEG-based materials are frequently used for the suppression of adhesion and settlement of biomolecules and bioorganisms [1–3, 7–9] and the fabrication of biologically inert templates that can be decorated with bioactive functional groups and specific receptors [10, 11]. For these applications, PEG moieties are used either as terminal parts of self-assembled monolayers (SAMs), in the form of oligo(ethylene glycols), or as the major or even only component of thin films. Such films can be prepared by different means, including spin-casting, drop-casting, or doctor blading of acrylate or isocyanate-decorated PEGs, dissolved in a suitable solvent, with the subsequent crosslinking of individual precursors. The crosslinking is usually mediated by either photochemical reactions triggered by exposure of the films to ultraviolet (UV) light [12–14] or by chemical coupling [15, 16], relying on the mutual affinity of specific coupling groups

embedded into the PEG precursors. As such precursors both linear and branched PEGs can be used, with the latter moieties being more suitable for efficient crosslinking [4]. Usually, these moieties, which are termed STAR-PEGs, are comprised of several PEG arms coupled together in the joint center and decorated with terminal groups, responsible for crosslinking or serving as specific receptors [17–21].

Along these lines, we applied four-arm STAR-PEGs, decorated with either amino (STAR-NH$_2$) or epoxy (STAR-EPX) terminal groups, which are complementary to each other, to the fabrication of ultrathin PEG films on different substrates. These films were found to possess distinct bioinert and hydrogel properties, which are important for applications. However, in contrast to most studies, dealing with bulk hydrogels [22–24], these properties were attributed to nanometer-thin PEG films, providing additional options for nanofabrication and design of hybrid materials. Moreover, it was possible to separate the PEG films from the primary substrate and obtain them as free-standing nanosheets, which could be either transferred to a secondary substrate or spanned over an opening. These nanosheets retained all favorable properties of the primary films, providing even more options for applications, also in combination with electron beam and UV lithography.

The present manuscript reviews the fabrication, properties, and applications of the STAR-PEG-based hydrogel films and nanosheets (PHFs and PHNs, respectively), providing specific

---

information in respect to the above issues and giving representative examples of applications in the context of nanofabrication, hybrid materials, and sensing. The fabrication and basic properties of the PHFs will be described in the next section, followed by the description of the PHNs (section 3), the effect of the molecular weight (MW) of the precursors (section 4), hybrid PHNs and PHNs (section 5), and their reaction to the electron (section 6), and UV (section 7) irradiation. The examples of applications will be provided in sections 8–13, followed by conclusions (section 14).

2   PHFs: Fabrication and basic properties

The PHF fabrication procedure is illustrated in Fig. 1 [25]. Schematic of the fabrication route is presented in Fig. 1(a). The STAR-NH$_2$ and STAR-EPX precursors, available commercially (Creative PEGWorks USA), are dissolved in chloroform at a fixed concentration, mixed, spin-coated onto the substrate (Au or Si wafer), crosslinked by thermal annealing (6 h, 80 °C), and finally rinsed extensively with ethanol to remove possible weakly bound material. The MW of the precursors was selected as 2000 (2k), 5000 (5k), 10,000 (10k), and 20,000 (20k) g/mol, corresponding to 9-11, 25-27, 50-55, and 100-112 EG monomers, respectively, with the lengths of the PEG arms of 3.5–3.9, 8.7–9.8, 17.5–19.5, and 35–39 nm. For most of the experiments, the precursors with a MW of 2k were used. The use of the other MWs will be specifically discussed in section 4 [26]. The mixing of the precursors was performed usually in the 1:1 ratio (wt./wt.), but deviations from this "stoichiometric" composition were used as well, as far as this was necessary for a specific test or application [27–30]. The thermally-promoted reaction between the terminal amino and epoxy groups of the precursors led to the appearance of ethanol-amine-like crosslinking bonds between the precursors (Fig. 1(c)), resulting finally in the creation of a porous PEG matrix, kept together by these bonds (Fig. 1(d)).

The crosslinking reaction between the STAR-NH$_2$ and STAR-EPX precursors occurs per the second-order kinetics, as follows from the monitoring of the characteristic vibration band of the epoxy group by infrared (IR) spectroscopy (Fig. 2(a)) [25]. Such a rate law corresponds to the expectation and excludes a possible thermal degradation of epoxy which would correspond to a first-order kinetics. Significantly, the monitored vibration band is not perceptible anymore after 3 h of the crosslinking reaction, which underlines the completed character of this reaction, involving the vast majority of the available amino and epoxy groups.

The PHF thickness can be flexibly adjusted in the 5–280 nm range by setting the concentration of the precursors in the primary solutions between 0.75 and 30 mg/mL (Fig. 2(b)) [25]. Significantly, the fabricated films are extremely robust and lose only a small amount of material upon such a harsh procedure as post-preparation ultrasonication (Figs. 2(b) and 2(c)). Whereas the absolute amount of the released PEG material does not depend on the film thickness, the relative amount becomes noticeably higher for the thinner films (Fig. 2(c)). The most obvious reason for this behavior is a lower extent of crosslinking in the latter films. Consequently, concentrations of the precursors above 5–8 mg/mL, corresponding to the more robust thicker PHFs, are preferable.

The bioinert properties of the PHFs were tested by X-ray photoelectron spectroscopy (XPS), relying on the characteristic N 1s signal of the proteins tested, viz. fibrinogen and avidin [25]. A strong decrease in the amount of the adsorbed proteins with increasing PHF thickness is observed, so that the PHFs with a thickness exceeding 20 nm are almost fully resistant to the absorption of avidin, whereas a small amount of fibrinogen is still recorded, presumably, due to its trapping in the PEG matrix (Fig. 2(d)).

The hydrogel properties of the PHFs were tested by varying the relative humidity (through temperature variation) and monitoring their thickness [25]. To this end, the PHFs were successively cooled down, in a step-like fashion, resulting in their swelling (Fig. 2(e)). The respective swelling ratio is shown in Fig. 2(f) as a function of the PHF thickness (d). This ratio is nearly constant at d > 30 nm but increases linearly with decreasing thickness for the thinner films (Fig. 2(f)). The reason for such behavior of the thinner films is once more the lower extent of crosslinking, making the swelling easier.

3   PEG nanosheets

A particular advantage of the STAR-PEG-based PHFs is the possibility of their separation from the substrate in the form of
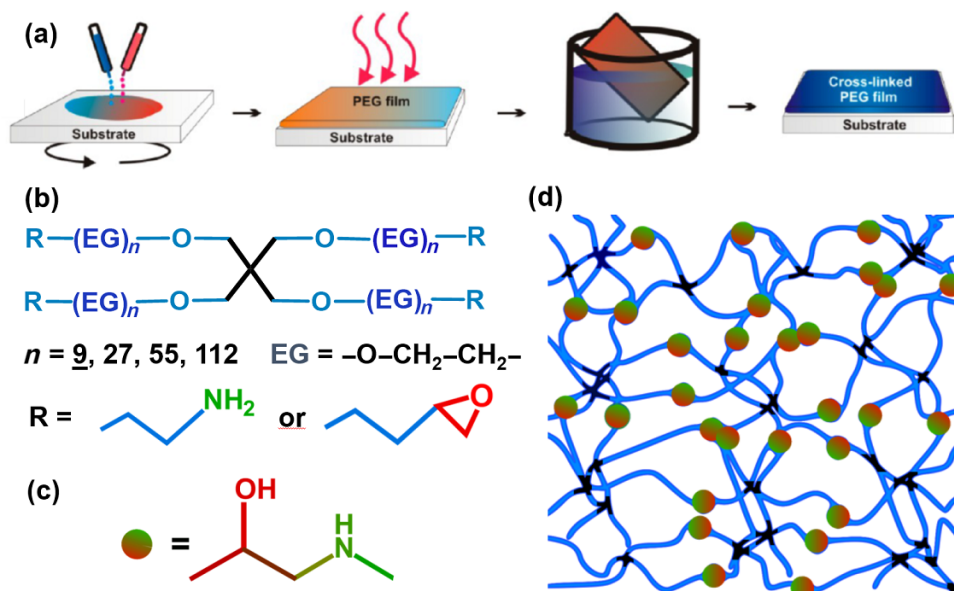

Figure 1   (a) Schematic of the PHF fabrication route. Reproduced with permission from Ref. [25], © American Chemical Society 2013. (b) The structure of the STAR-NH$_2$ and STAR-EPX precursors. (c) Ethanol-amine-like crosslinking bond resulting from the reactions between the terminal epoxy and amino groups of the precursors. (d) Schematic of the PEG matrix, kept together by the crosslinking bonds. Reproduced with permission from Ref. [26], © American Chemical Society 2021.
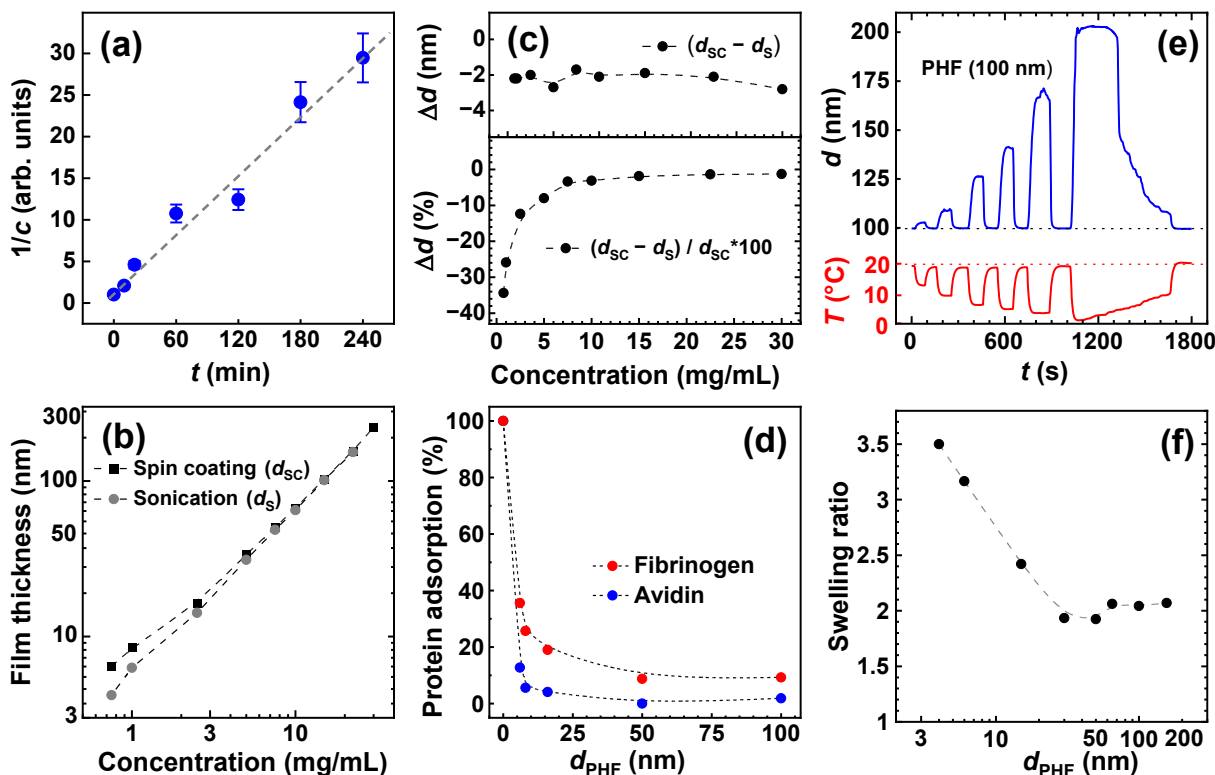
Figure 2 (a) Inverse intensity of a characteristic IR band of epoxy plotted as a function of the reaction time during the PHF formation. (b) The thickness of the PHFs after the spin-coating (black squares) and subsequent ultrasonication (grey circles) as a function of the precursor concentration in the primary solution. (c) Absolute (top panel) and relative (bottom panel) material loss upon ultrasonication. (d) Normalized protein content as a function of the PHF thickness. (e) Thickness variation during multiple swelling steps of a 100 nm PHF (top panel) as a response to the temperature variation (bottom panel). (f) Swelling ratio of a 100 nm PHF as a function of its thickness. Reproduced with permission from Ref. [25], © American Chemical Society 2013.

PHNs, which can compete with other types of organic and hybrid nanosheets [31–36] but feature a variety of specific favorite properties. For this purpose, two procedures were developed. Within the first procedure, illustrated in Fig. 3(a), PHFs are prepared on a thin (100 nm) Au film, evaporated onto a silicon substrate without a commonly used, intermediate titanium adhesion layer [37]. The PHF/gold bilayer can then be separated easily from the silicon substrate by an oblique immersion in water. Afterward, the sacrificial gold layer is dissolved by a proper etchant [38, 39], releasing a PHN. Within the second procedure, PHFs are prepared on SiO_2-passivated Si wafers, exposed to HF vapor to diminish their bonding to the substrate by the removal of

the SiO_2 overlayer, and separated from the substrate by an oblique immersion in water [28]. The released PHN can then be transferred to a secondary substrate or a supporting mesh. An example of free-standing PHN (50 nm) spanned upon 350 nm × 350 nm openings of the supporting mesh is shown in Fig. 3(b). An example of a transferred PHN (100 nm), on a secondary substrate, is presented in Fig. 3(c), along with an atomic force microscopy (AFM) height profile across its edge in Fig. 3(d).

The most straightforward application of the PHMs is bioinert support for high-resolution transmission electron microscopy (HRTEM). An example of such imaging, for an iron storage protein, ferritin, is presented in Fig. 3(e). The fine structure of the
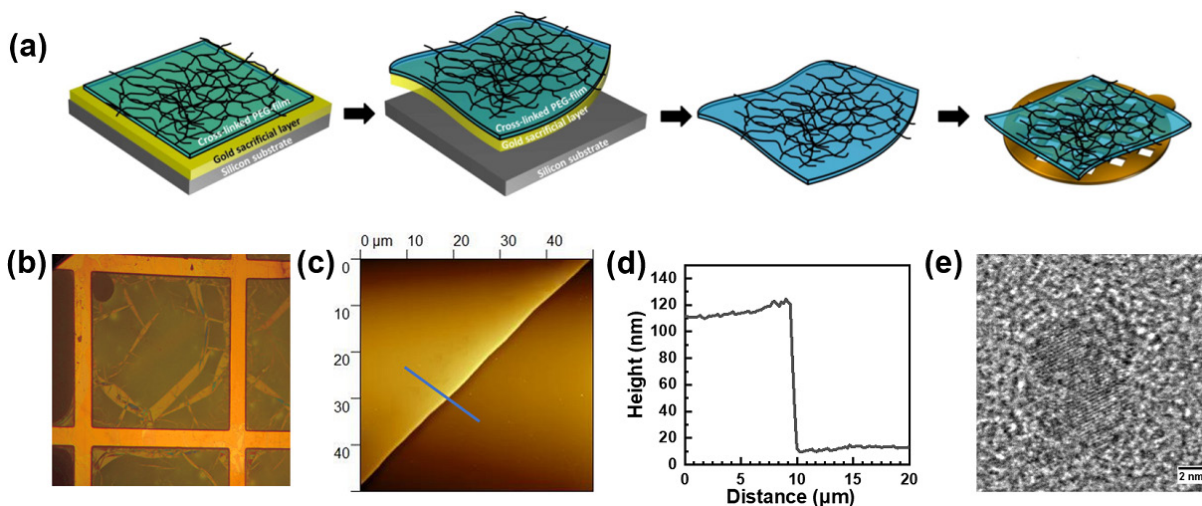

Figure 3 (a) Schematic of the PHN fabrication route. (b) Free-standing 50 nm PHN supported by a mesh with 350 nm × 350 nm openings. (c) AFM image of a PHN (100 nm) transferred onto a Si substrate. (d) The height profile across the edge of this PHN, along the blue line in (c). (e) HRTEM image of the iron core of ferritin, an iron storage protein, supported by a PHN (50 nm). (a) and (e) Reproduced with permission from Ref. [37], © WILEY-VCH Verlag GmbH & Co. KGaA, Weinheim 2014. (c) and (d) Reproduced with permission from Ref. [26], © American Chemical Society 2021.

crystalline ferrihydrite core of this protein is well distinguishable. The quality of the image is comparable with those of ferritin deposited on distinctly thinner single-sheet graphene oxide [40] or PEG-modified carbon nanosheets [31].

The PHNs retain the original bioinert and hydrogel properties of the parent PHFs, featuring at the same time exceptional elastic properties [37, 28]. The latter properties were monitored by the bulge test [41]. For this purpose, PHNs were suspended over the square or circular window and subjected to pressure. For a circular window with a radius a (Figs. 4(a) and 4(b)), the relation between the pressure difference on both sides of the nanosheet (Δp), and its deflection (h) is given by Eq. (1) [42]

$$\Delta p = 4\frac{t}{a_2}\sigma_0 \cdot h + \frac{8}{3}\frac{d}{a^4} \cdot \frac{1}{1-v}E h^3 \quad (1)$$

where σ_0 is the residual stress, v is the Poisson's ratio, d is PHN thickness, and E is the Young's modulus. Plotting $\Delta p/h$ vs. h^2 the value of E could be determined (Fig. 4(c)). It was extremely small compared to analogous nanosheets made of other materials [37], varying only slightly (from 2.05 to 2.6 MPa) at the PHN thickness variation [28]. The high elasticity of the PHNs was attributed to the elastomer character of the PEG matrix, with fixed crosslinking nodes and interconnecting PEG chains, stretching easily upon a load. Very important is the fact that not only the PHNs featuring the optimal ("stoichiometric") mixing ratio of the STAR-NH$_2$ and STAR-EPX precursors (1:1) but also the nanosheets featuring non-stoichiometric mixing ratios are sufficiently stable and show similar elastic properties (Fig. 4(e)).

4 Effect of molecular weight

Whereas most of the experiments were performed with an MW of the precursors of 2000 (2k) g/mol (all other sections), larger MWs, viz. 5000 (5k), 10,000 (10k), and 20,000 (20k) g/mol, available commercially, were tested as well (this section) [26]. Stable PHFs with adjustable thickness (10–330 nm) could be formed in a broad concentration range of the precursors, with progressively larger thickness with increasing MW at a fixed concentration (Figs. 5(a) and 5(b)). All these films exhibit distinct hydrogel properties, but the swelling ratio decreases to some extent with increasing MW (Fig. 5(c)). Independent of the MW, the PHFs also show persistent bioinert properties at a sufficiently high thickness, as evidenced by the protein adsorption test (Fig. 5(c)). In contrast, at a low thickness, such as 50 nm, protein adsorption increases strongly with increasing MW, which, however, does not mean a

degradation of bioinertness but is a consequence of the progressively increasing PHF porosity, defined by the length of the PEG arms (see section 2). At a high porosity, proteins can penetrate through the thin films and adsorb at the protein-adhesive substrate.

Along with the PHFs, PHNs could also be fabricated in the entire MW range [26]. Unexpectedly for the elastomer model, their Young's modulus does not decrease but increases with increasing MW (Fig. 5(e)), which was tentatively explained by the MW-dependent extent of coiling for the interconnecting PEG chains in the matrix [26]. All PHNs exhibit similar deformation at a specific Δp (bulge test), given by the thickness reduction, but their stability increases with decreasing MW (Fig. 5(c)), which is understandable given the higher density of crosslinking points.

5 Hybrid films and membranes

Due to their hydrogel properties and porous character, PHFs and PHNs can serve as a versatile platform for hybrid materials. Among other options, they can be loaded with nanoparticles (NPs) [25, 43]. The easiest procedure in this context is the immersion of the PHFs into an aqueous solution of NPs; a representative scanning electron microscopy (SEM) image of a respective hybrid film is shown in Fig. 6(a). A special characteristic of such films is an inhomogeneous distribution of the NPs within the films, with the highest density at the film/ambient interface [25]. A homogeneous distribution can be achieved by the introduction of NPs into the precursor solution, denoted one-pot procedure. The hydrogel properties of the PHFs become somewhat deteriorated by the NP loading, with, as expected, a larger effect in the case of the one-pot procedure (Fig. 6(b)).

Another example of hybrid materials is C60-loaded PHFs and PHNs [44]. Along with the immersion and one-pot procedures, the so-called reflux approach, relying on the chemical coupling of C60 to the amino group of the STAR-NH$_2$ precursors, was used. In all cases, C60 formed clusters (190–310 nm) which become distributed in the PEG matrix, as was in particular shown by AFM imaging (Fig. 6(c)). The C60 content and the electronic structure of the C60-PEG composites depended on the preparation procedure, as shown by the UV–visible (UV–vis) spectra (Fig. 6(d)). Whereas the intensity of the absorption signal represents a measure of the former parameter, its position is assumed to be related to the local intermolecular distances between fullerenes in their supramolecular aggregates.

Significantly, the electrochemical properties of C60 are preserved in the PEG matrix, as evidenced by the characteristic
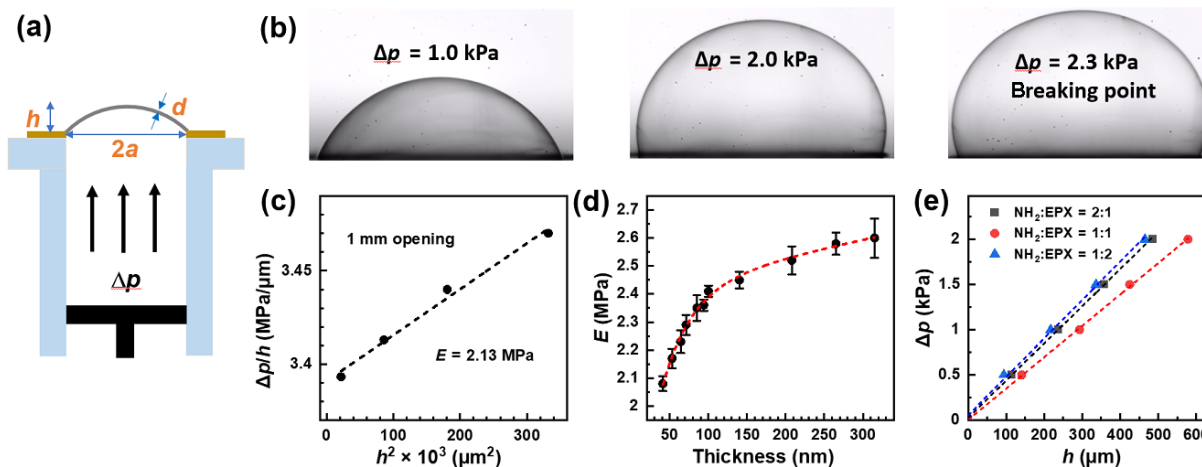

Figure 4 (a) Schematic illustration of the bulge test setup and relevant parameters (see text for description). (b) Selected optical images of the deflected PHN (100 nm), suspended over a circular window with a diameter of 1 mm. (c) $\Delta p/h$ vs. h^2 plot for this PHN. (d) Dependence of the Young's modulus on the PHN thickness. (e) Δp vs. h plots for the PHNs (100 nm) prepared at the different mixing ratios of the STAR-NH$_2$ and STAR-EPX precursors, as shown in the legend. Reproduced with permission from Ref. [28], © Zhao, Z. Y. et al. 2022.
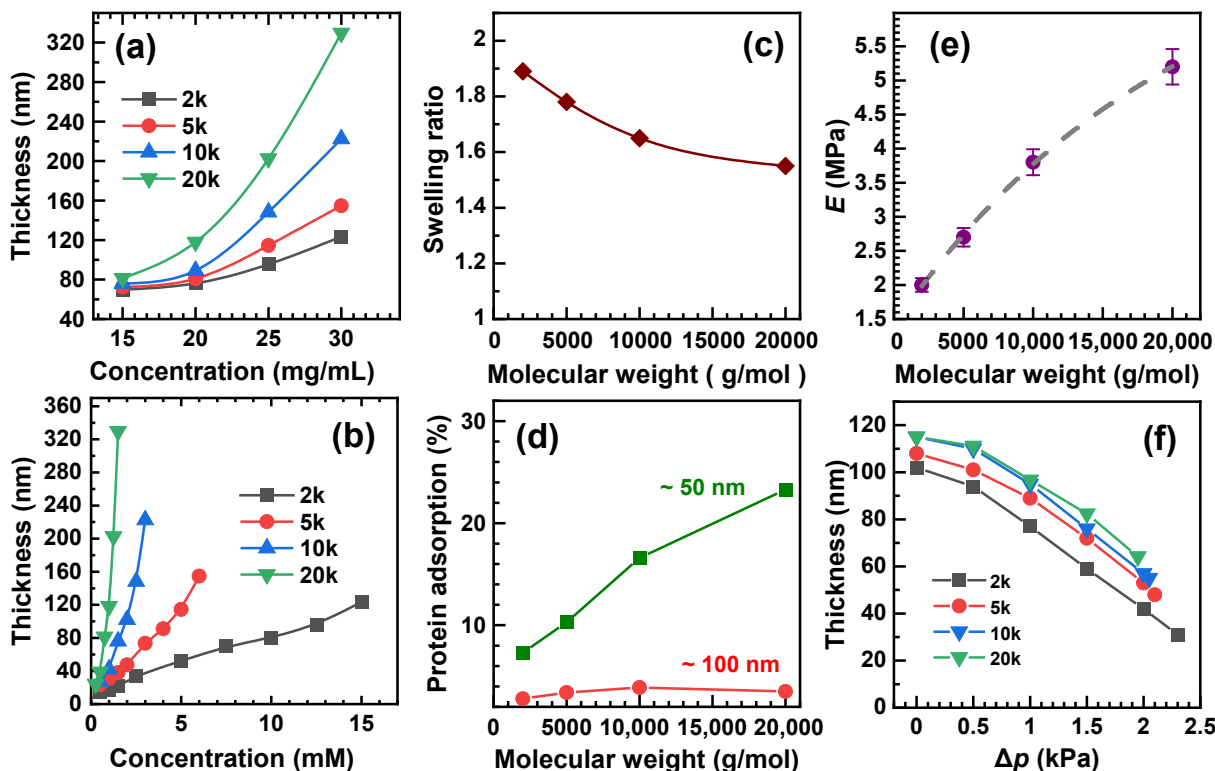
Figure 5 (a) and (b) The thickness of the PHFs formed by the precursors with different MWs as a function of their concentration in the primary solutions, given in either mg/mL or mM. (c) Swelling ratio of a PHN (100 nm) vs. the MW. (d) Relative protein absorption vs. the MW for the PHFs with ~ 50 and ~ 100 nm thicknesses. (e) Young's moduli of the PHNs (100 nm) vs. the MW. (f) Variation of the PHN thickness during the bulge test. Reproduced with permission from Ref. [26], © American Chemical Society 2021.
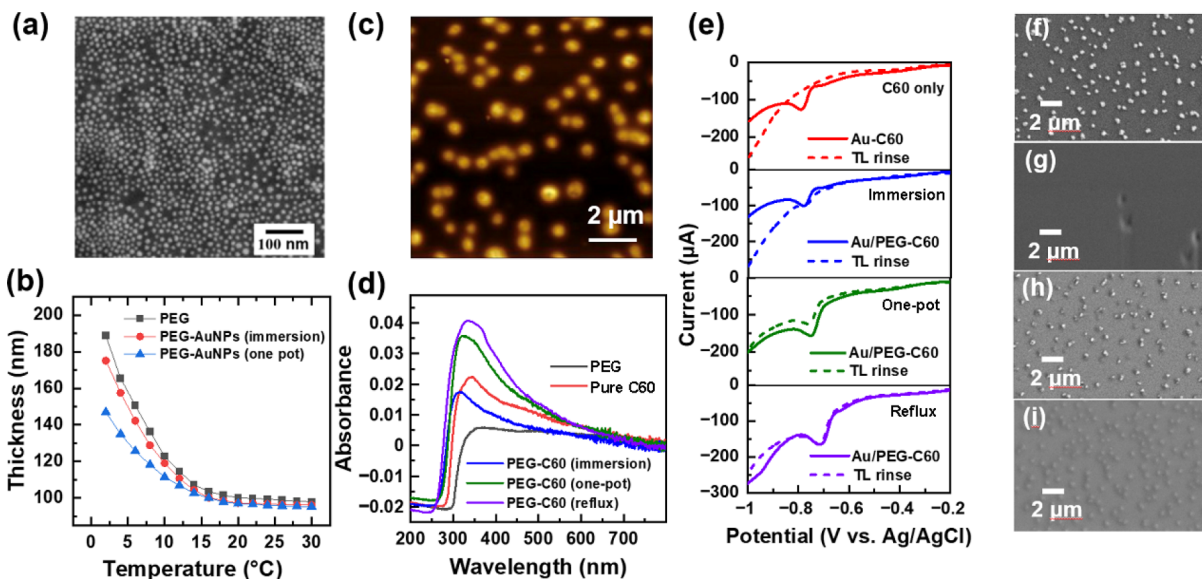

Figure 6 (a) SEM image of a PHN (40 nm) loaded with AuNPs (13 nm). Reproduced with permission from Ref. [43], © American Chemical Society 2015. (b) Swelling of pristine and AuNP-loaded (15 nm) PHFs at increasing humidity triggered by the decreasing temperature. (c) AFM image of C60-loaded PHFs. (d) UV–vis spectra of pristine and C60-loaded PHFs. (e) SWV curves for C60/Au and C60-loaded PHFs on Au. (f)–(i) SEM images of C60-loaded PHFs on Au prepared by (f) and (g) immersion and (h) and (i) reflux procedures (f) and (h) before and (g) and (i) after TL rinse. Reproduced with permission from Ref. [44], © American Chemical Society 2023.

[45, 46] reductive peak at –0.8 V in the square wave voltammetry (SWV) curves (Fig. 6(e)). Interestingly, this peak disappears completely or becomes attenuated to some extent after the rinse of the C60-PEG composites prepared by the immersion and one-pot procedures, respectively, by toluene (TL)—a good solvent for C60 (Fig. 6(e)). Consequently, only the composites prepared by the reflux procedure are sufficiently robust and stable, as also confirmed by the SEM images acquired before and after the TL rinse (Figs. 6(f)–6(i)).

6 Modification by electron irradiation

PHFs and PHNs can be modified by electron irradiation, which offers additional options for lithography and nanofabrication [28, 47, 48]. The electron irradiation results in significant chemical modification and partial desorption of the PEG material (Fig. 7(a)), as in particular follows from the evolution of the C 1s XPS spectra, in which the peak associated with the pristine PEG material decreases in intensity, while a new peak, related to the modified (carbon-enriched and oxygen-depleted) PEG material
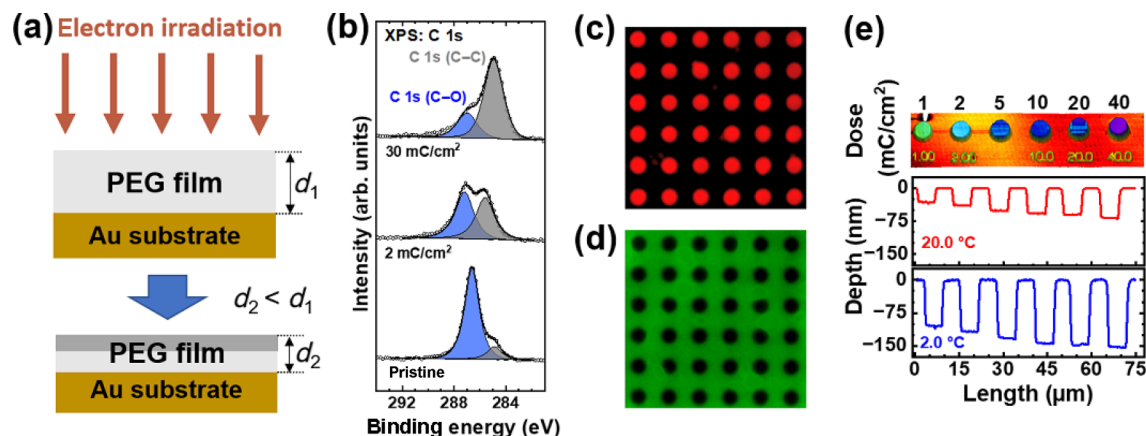
Figure 7 (a) Schematic of the PHF modification by electron irradiation. The chemically modified PEG material is shown in dark gray. Reproduced with permission from Ref. [49], © Zhao, Z. Y. et al. 2021. (b) C 1s XPS spectra of pristine and irradiated (50 eV) PHFs. The spectra are decomposed into contributions associated with the pristine (blue) and chemically modified (gray) PEG material. (c) and (d) Fluorescence microscopy images of EBL patterned PHFs (50 nm) after immersion into a phosphate buffered saline (PBS) buffered solution of fluorescently labeled fibrinogen (c) and an aqueous solution of fluorescein (d). (e) AFM image (3D) of a circular pit array written in PHF (100 nm) with different doses (top panel), along with the corresponding height profiles across the array, recorded at 20 °C (middle panel) and 2 °C (bottom panel). Reproduced with permission from Ref. [47], © American Chemical Society 2013.

appears and increases in intensity (Fig. 7(b)). The modified material loses bioinert and hydrogel properties, which, in combination with electron beam lithography (EBL), can be in particular used to create protein and dye patterns. Whereas proteins exclusively adsorb within the EBL-modified, protein-adhesive areas (Fig. 7(c)), dyes, dissolved in water, are only adsorbed outside of these areas, relying on the hydrogel properties of the pristine PEG material (Fig. 7(d)).

EBL can be used for three-dimensional (3D) (morphology) patterning of the PHF templates. An example of such a pattern is given in Fig. 7(e). It is a circular pit array, with a depth of a pit set by the applied irradiation dose, as visualized by the height profile across the array taken at 20 °C. An increase of the relative humidity, triggered by the temperature drop to 2 °C, results in the swelling of the 3D pattern, as shown by the respective height profile in Fig. 7(e). Significantly, the swelling involves only the pristine part of the pattern, whereas the EBL-modified parts are not affected because of the loss of the hydrogel properties.

7 Modification by UV light

PHFs and PHNs can also be modified by UV light [28, 49]. In contrast to electrons, the only effect of such an irradiation is

progressive decomposition of the PEG material followed by immediate desorption of the released fragments (Fig. 8(a)). The residual PEG material does not change its chemical composition, as in particular evidenced by the persistence of the characteristic C 1s XPS signal (Fig. 8(b)). Accordingly, the hydrogel and bioinert properties of this material remain unchanged, as evidenced by the invariable swelling ratio (Fig. 8(c)) and invariable lack of protein adsorption for sufficiently thick PHFs (Fig. 8(d)). Only for thin PHFs, a slight increase of protein adsorption during the UV treatment is observed (Fig. 8(d)), related to the progressive protein diffusion through the porous PEG matrix to the protein-adhesive substrate. In combination with lithography, all-PEG 3D patterns can be fabricated, as shown by a representative example (proximity printing) in Figs. 8(e) and 8(f). These patterns are distinctly different from the EBL ones, combining pristine and modified PEG.

8 Temperature sensors

The versatile properties of PHFs and PHNs make possible a variety of applications. A representative example in this context is temperature sensor relying on the PEG-AuNP composite films prepared by the immersion procedure [25]. The optical
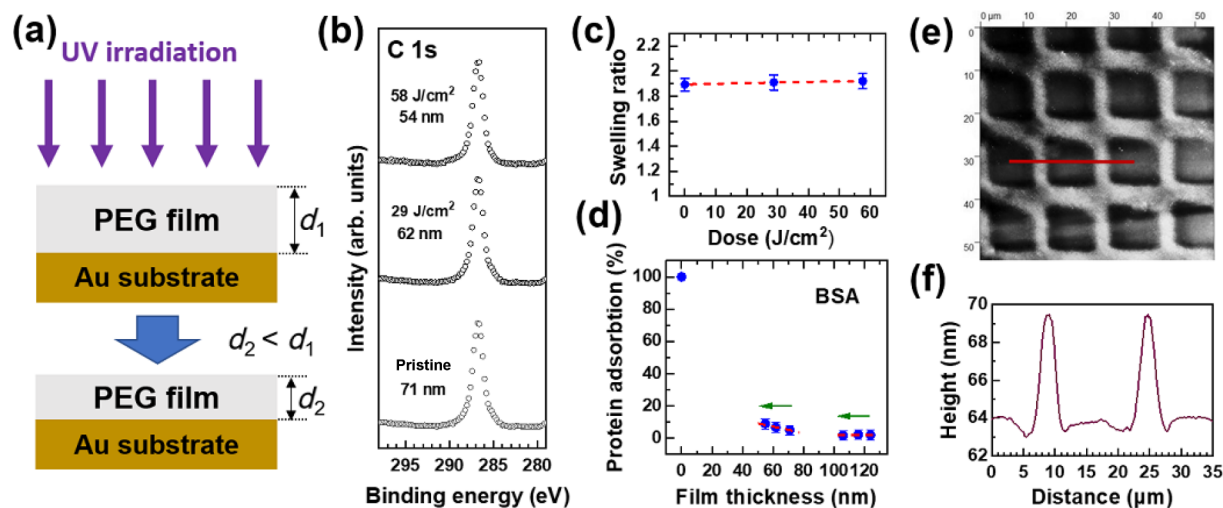

Figure 8 (a) Schematic of the PHF modification by UV light. (b) C 1s XPS spectra of pristine and irradiated (254 nm) PHFs. (c) PHF (71 nm) swelling ratio vs. irradiation dose. (d) Relative extent of the BSA adsorption for the 71 and 124 nm PHFs subjected to UV irradiation. The direction of the thickness variation during the UV treatment is shown by the arrows. (e) AFM image of a representative pattern fabricated with a dose of 28.8 J/cm². (f) Height profile along the red line in the AFM image. Reproduced and adapted with permission from ref. [49], © Zhao, Z. Y. et al. 2021.

appearance of these films changes noticeably upon temperature-induced swelling (Fig. 9(a)), which was also monitored by UV–vis spectroscopy (Fig. 9(b)). The intensity of the characteristic local surface plasmon resonance (LSPR) band of AuNPs exhibits a progressive decrease with decreasing temperature (Fig. 9(c)), making the initially violet PEG-AuNP film transparent so that the gold substrate becomes visible. This behavior is explained by the inhomogeneous distribution of the NPs in the PHF in the case of immersion (section 5). The AuNPs are predominantly located at the PHF/ambient interface and the behavior of the LSPR band depends on the interaction between these NPs and the conductive substrate (gold), following literature reports [50–52]. This interaction changes with the increasing distance between the NPs and the substrate (Fig. 9(d)), resulting in the observed change in the optical spectrum. Of course, the temperature range covered by this sensor is limited but its simplicity and direct character make it useful, e.g., in the context of food storage.

9   Pattern transfer

A combination of EBL and hydrogel properties of the PHFs and PHNs provides a unique opportunity to create NP patterns on non-flat and/or non-conductive supports with the EBL precision [47]. Initially, a PHF is prepared on a primary, conductive substrate and patterned by EBL (Fig. 10(a)). Afterward, the patterned PHF is separated from the primary substrate in the form of PHN and transferred to the secondary, non-flat, and/or non-

conductive support. Then, the PHN template is exposed to NPs, which mimics the pattern, adsorbing only within the pristine PEG areas. Finally, the PEG matrix is removed by hydrogen plasma treatment, leaving the desired NP pattern (Fig. 10(a)).

As an example, an AFM image of a glass-supported PHN template with a pattern of a QR code after transfer from the primary conductive support is presented in Fig. 10(b). Regions exposed to electron beam appear ~ 17 nm deeper than the pristine background (Fig. 10(d)). The modified material within these regions does not possess hydrogel properties so that the AuNP adsorption occurs beyond these areas. The resulting AuNP pattern becomes well-visible after the PEG matrix removal, mimicking the original EBL pattern (Fig. 10(c)). The high precision of EBL is conserved, as shown by a magnified image of an element of this pattern (Fig. 10(e)).

10   Humidity sensors

Hydrogel properties of the PHFs and PHNs make them suitable for humidity sensing. This was realized with the resistive transduction technique, using the experimental setup shown in Fig. 11(a) [42]. Four-probe method with soft contact to the samples was applied and the relative humidity (RH) was precisely controlled by passing nitrogen gas flow through two parallel-adjusted PYREX gas washing bottles filled with pure water and concentrated sulfuric acid. Both pristine and NP-loaded PHNs, transferred to the insulating glass support, were tried. The
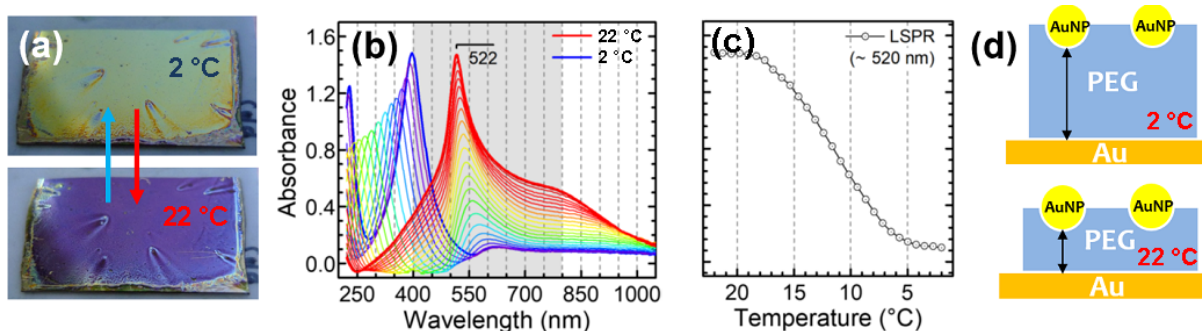

Figure 9   (a) Influence of temperature-induced swelling on the optical appearance of the PEG-AuNP composite films. (b) Consecutive UV–vis spectra acquired in the course of temperature-induced swelling. (c) Strong decrease in the intensity of the LSPR band as a function of temperature, i.e., the extent of swelling. Reproduced with permission from Ref. [25]. © American Chemical Society 2013. (d) Schematic of the swelling effect on the distance between the AuNPs and Au substrate.
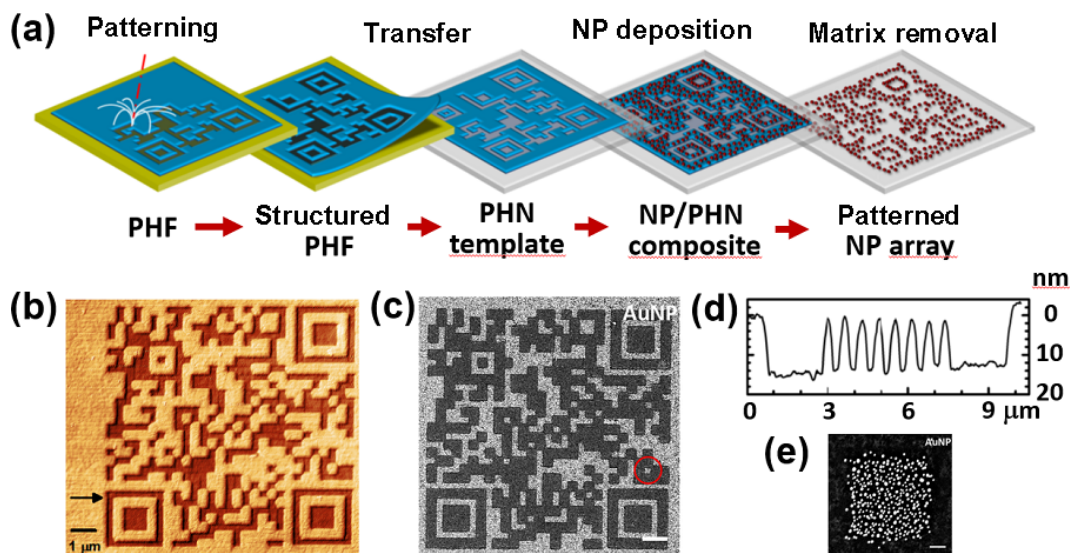

Figure 10   (a) Schematic representation of the preparation process for tailor-made NP patterns on arbitrary substrates by means of a transient PHN template (60 nm). (b) AFM image of a glass supported PHN template with pattern of a QR code (29 by 29 modules) after transfer from the primary conductive support. (c) SEM image of this pattern after the AuNP (35 nm) loading and PHN removal. (d) Height profile across (b) as shown by the black arrow. (e) An element of the image in (c) is marked by the red circle. Reproduced with permission from Ref. [48], © American Chemical Society 2014.
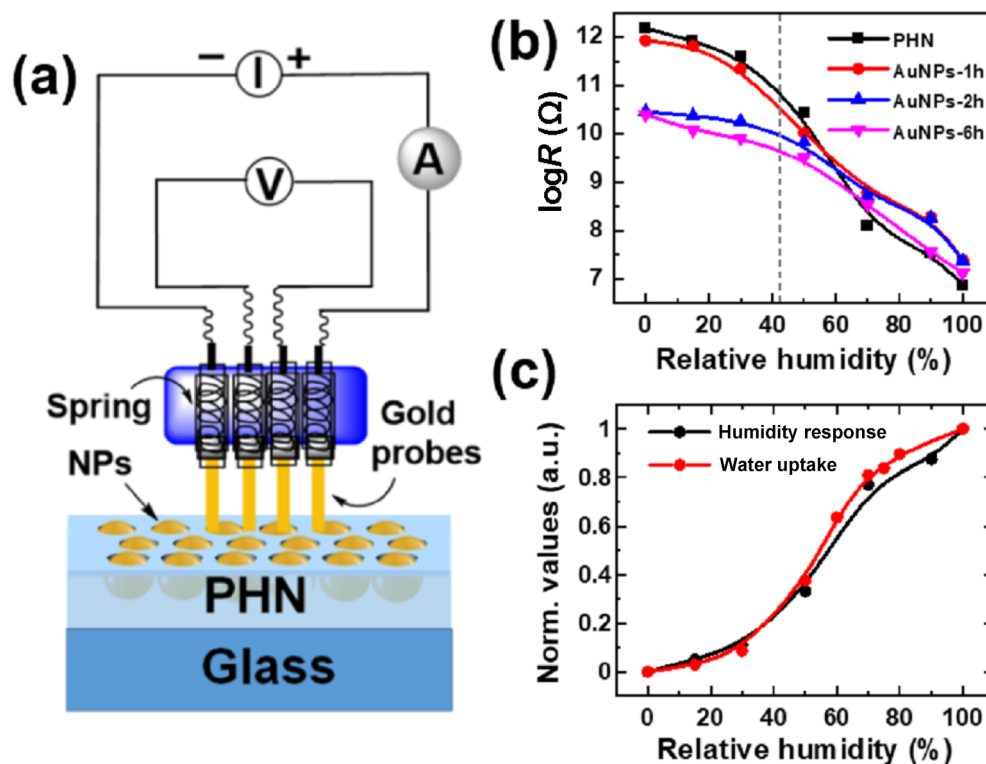
Figure 11 (a) Schematic representation of the experimental setup to measure the PHN conductivity. (b) Normalized resistance of the pristine and AuNP (13 nm) loaded PHNs as a function of RH. (c) Normalized humidity response and water uptake for the pristine PHN as functions of RH. Reproduced (panels b and c) with permission from Ref. [43], © American Chemical Society 2015.

concentration of the NPs in the PEG-NP composite nanosheets was varied by setting the immersion time for the NP solution. The resistance of the pristine membrane was found to change by ~ 5.5 orders of magnitude upon RH variation from 0% to 100% (Fig. 11(b)), which is an unprecedented response for homogeneous materials. The introduction of the NPs increased the conductivity but diminished this response (Fig. 11(b)), so that the pristine PHN was considered as preferable. It was assumed that the dependence of resistance on the water uptake into the pristine PHN, $U(RH)$, is approximately described by the exponential function. This assumption was supported by the correlation of $\log R_{dry} - \log R(RH)$ with $U(RH)$, determined as the difference in the PHN thickness at a certain RH and in the dry state (Fig. 11(c)). The exponential dependence of resistance on the water uptake means a much higher sensitivity of the PHN humidity sensor compared with the standard ones, for which a linear correlation is usually recorded [53].

Note that the conductivity of the PHNs has most likely a predominant ionic character [54]. The use of the DC approach instead of AC methods, frequently used in such cases [55], could then in principle lead to electrolytic effects and polarizing a system. However, such behavior was not observed; all recorded resistance values were stable over time and well-reproducible at repeating measurements [42].

11   Protein sensors

The bioinert character of the PEG matrix makes the PHFs and PHNs suitable as a bioinert platform for biosensors, including recognition of specific proteins in particular, which is an important task in the context of bioengineering and medicine [56−58]. For this purpose, specific protein receptors should be embedded into the PEG matrix, coupling to it chemically. Such a coupling can be performed either via free amino or epoxy groups in the matrix. However, the density of these groups is quite low because most of the reactive groups of the PEG-NH$_2$ and PEG-

EPX precursors participate in the crosslinking, building ethanol-amine-like crosslinking bonds (see section 2). This situation, however, is only characteristic of the stoichiometric mixing ratio of the precursors (1:1), and the density of the reactive amino or epoxy groups can be increased noticeably at non-stoichiometric mixing ratios. Significantly, the PHFs and even PHNs (see section 3) retain their properties and stability at the latter conditions [27, 28].

Taking the above considerations into account, we introduced the avidin/streptavidin-specific biotin receptors into the PHF matrix by using the reaction between the free amino group in this matrix and N-hydroxy succinimide (NHS) ester groups of NHS-biotin (Fig. 12(a)). The density of the free amino groups was varied by the variation of the mixing ratio of the precursors. The PEG-biotin films were then subjected to both specific (avidin) and nonspecific (bovine serum albumin (BSA) and albumin) proteins (Fig. 12(a)). The outcome of the protein adhesion was monitored by XPS, relying on the characteristic N 1s signal of the proteins. Because of the limited sampling depth of XPS [59], the measurements could only be performed for quite thin PHFs (23–35 nm), so that a partial diffusion of the proteins across the films and their adsorption at the PHF/substrate interface could not be completely excluded. The derived data show a high preference for the adsorption of the specific protein and a distinct dependence of the protein density on the PHF composition (Fig. 12(b)). The adsorption of the non-specific proteins could not be completely avoided but was most likely related to their diffusion to the substrate, followed by their adsorption at the PHF/substrate interface (see above).

12   DNA sensors

Another important class of biomolecules is DNA. The development of reliable and sensitive methods for DNA sensing is crucial for creation of efficient diagnostic tools and advancements in medicine and biotechnology [60−64]. In this context, we
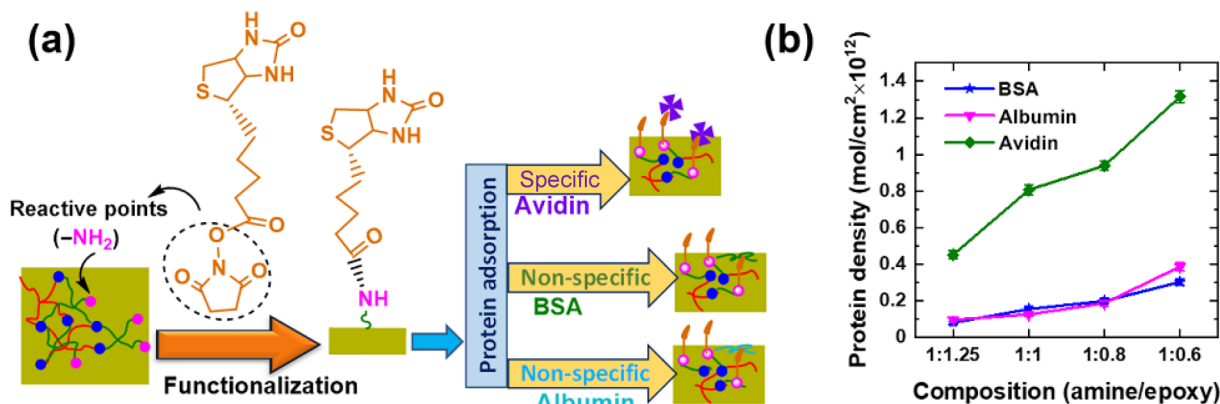
Figure 12 (a) Schematic representation of the experimental approach. (b) Grafting density of specific (avidin) and nonspecific (bovine serum albumin (BSA) and albumin from chicken egg white) proteins for a series of PHFs (23–35 nm) functionalized with NHS-biotin. The composition of the precursors, given by the amino/epoxy ratio, was varied. Reproduced with permission from Ref. [27], © The Royal Society of Chemistry 2016.

fabricated model, single-strand DNA (ssDNA) sensors on the basis of the PHFs and PHNs [29, 30]. As an established test system [65–69], we used complementary thymine (T) and adenine (A) homo-oligonucleotides, with either 5 (T5 and A5) or 10 (T10 and A10) bases. Tn were used both as the probe strands and mismatching target strands, while An were used as the matching target strands (Figs. 13(a) and 14(a)). Two different strategies for immobilization of the probe ssDNA into the PEG matrix were applied. Within the first strategy [29], the NHS-functionalized Tn strands (Tn-NHS) were coupled to the free NH_2 groups in the PEG matrix (Fig. 13(a)), similar to the protein sensors (previous section). Within the second strategy [30], thiol-functionalized Tn strands (Tn-SH) were coupled to the free epoxy groups via the established thiol–epoxy click reaction that leads to the formation of a β-hydroxythio-ether linkage [70, 71] (Fig. 14(a)). The density of the free NH_2 and epoxy groups in the PEG matrix was adjusted accordingly, setting either 2:1 or 1:2 mixing ratio for the PEG-NH_2 and PEG-EPX precursors.

The efficient immobilization of the probe Tn-NHS and Tn-SH into the PEG matrix was confirmed by XPS, relying on the specific

spectroscopic signatures of the T nucleobase [67, 72]. The density of the probes could be varied by setting their concentration in the primary buffer solution. Complementary to XPS, immobilization and hybridization processes were monitored by electrochemical tools, including cyclovoltammetry (CV) and electrochemical impedance spectroscopy (EIS). These techniques do not require vacuum and complex equipment and can be easily implemented in any laboratory.

Representative data for the NH_2:T10-NHS coupling are presented in Figs. 13(b)–13(e). Both the CV curves (Fig. 13(b)) and the Nyquist plots (Fig. 13(c)) show nearly no changes upon the exposure of the Au/PEG:T10-NHS working electrode to the mismatching T10 homo oligonucleotide. In contrast, there is a significant change upon exposure to the matching, A10 target sequence, corresponding to a hybridization efficiency of ~ 89%, as shown by XPS [29], relying on the specific spectroscopic signatures of the A nucleobase [67, 72]. This change is pronounced much strongly in the EIS case, so that this technique was selected as the most suitable one. To test the sensitivity of this technique, the concentration of A10 in the tested solution was
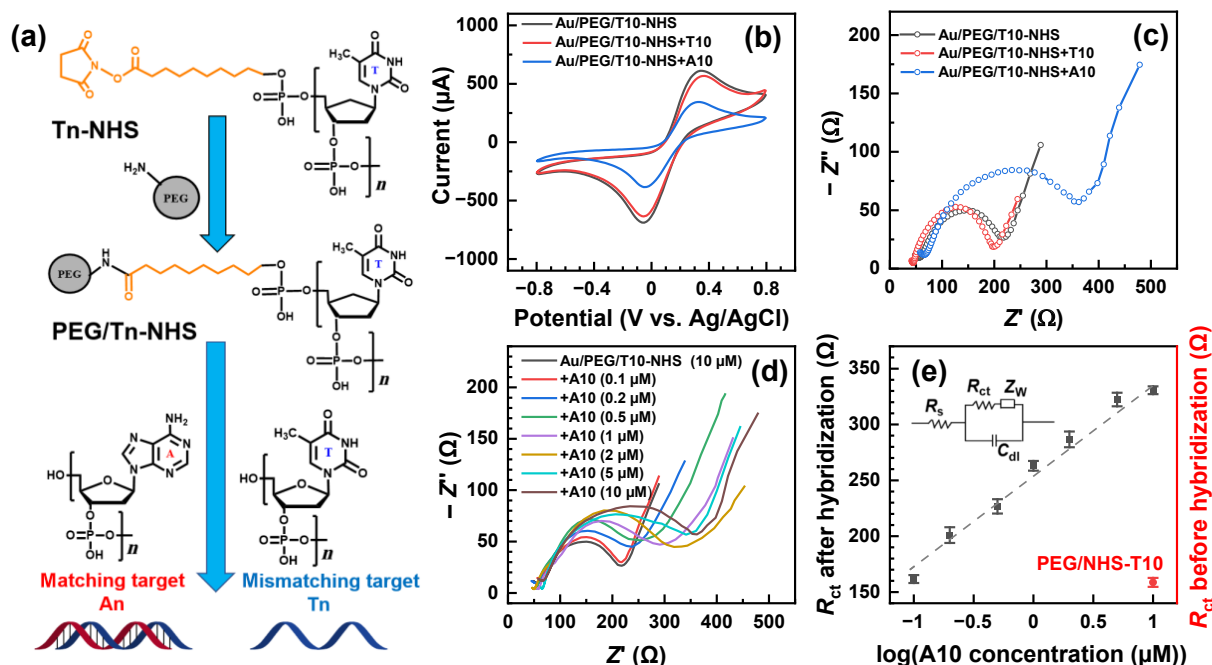

Figure 13 (a) The structures of the Tn-NHS, An, and Tn compounds as well as a schematic illustration of the Tn-NHS immobilization in the PEG matrix (shown schematically as a gray circle) via the free NH_2 groups and its subsequent reaction with the An and Tn targets. (b) and (c) CVs and Nyquist plots for the Au/PEG:T10-NHS working electrode before and after its exposure to mismatching (T10) and matching (A10) target ssDNA. (d) and (e) Nyquist plots and the derived R_{ct} values for the Au/PEG:T10-NHS working electrode before (red symbol in (e)) and after (black symbols in (e)) its exposure to matching A10 target ssDNA (variable concentration). The equivalent circuit is shown in panel (e). Reproduced with permission from Ref. [29], © Zhao, Z. Y. et al. 2022.
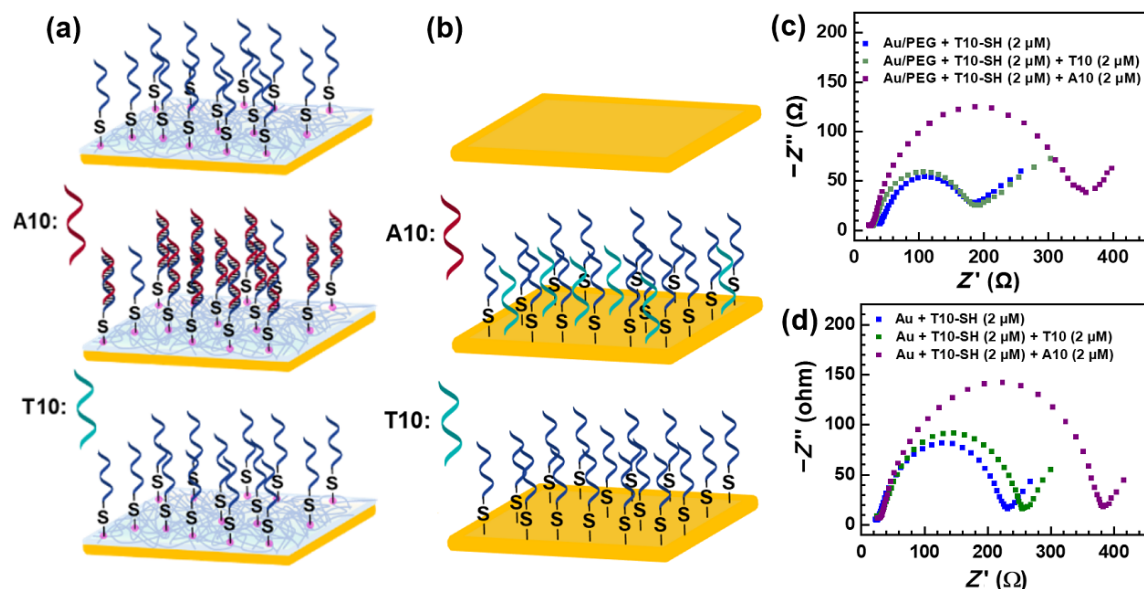
Figure 14 (a) and (b) Schematic representation of the experimental approach for the Au/PEG:ssDNA and Au/ssDNA sensors. (c) and (d) Nyquist plots for the Au/PEG:T10-SH and Au/T10-SH working electrodes before and after their exposure to mismatching (T10) and matching (A10) target ssDNA. Reproduced with permission from Ref. [30], © the Onwer Societies 2023.

varied and the EIS data were recorded. The respective Nyquist plots showed progressive variation with the varied concentrations (Fig. 13(d)). The evaluation of these data in terms of the equivalent circuit suggests that the most suitable fingerprint parameter for monitoring the hybridization efficiency (and also the efficiency of the probe ssDNA immobilization) is the charge transfer resistance, R_{ct}. The respective R_{ct} values are presented in Fig. 13(e) vs. A10 concentration. According to these data, the detection limit of the PEG:T10-NHS sensor to A10 is down to 0.1–0.2 µM.

A similar detection limit of 0.1 µM was also achieved in the case of epoxy-thiol coupling of the probe ssDNA strands [30]. This detection limit is quite reasonable and comparable with literature data for some other types of ssDNA sensors [73], even though it is still inferior to the most advanced sensors [74–76]. However, one can reasonably assume that the detection limit of the presented Au/PEG:ssDNA sensor can be improved even further, e.g. by a larger loading of the PEG film with the probe ssDNA.

The performance of the Au/PEG:ssDNA sensor, relying on the thiol-epoxy coupling, was compared with an established sensor fabricated by the "direct" assembly of thiolated ssDNA on gold substrates, following the standard procedure [66–69, 77, 78]. Similar, to the Au/PHF:ssDNA case, probe T10-SH strands were assembled directly on gold and used for the detection of the matching, target A10, with the additional selectivity test by mismatching T10 (Fig. 14(b)). Whereas this sensor was found to be equivalent to the Au/PHF:ssDNA case in terms of the hybridization efficiency (~ 85%), it exhibited lower selectivity for the target DNA sequence as seen by the comparison of the EIS data (Figs. 14(c) and 14(d)). Whereas the Au/PEG:A10-SH sensor shows no response to the mismatching T10 (Fig. 14(c)), there is a noticeable response in the case of Au/A10-SH (Fig. 14(d)). This behavior is most likely related to the presence of defects in the probe T10-SH monolayer, allowing direct contact of mismatching ssDNA with the gold substrate.

The high selectivity of the Au/PEG:ssDNA sensors with respect to the target ssDNA is primarily related to the bioinert character of the PEG matrix, preventing non-specific adsorption of non-target ssDNA. But also, the hydrogel character of this matrix is of importance, hindering further sensor biofouling. A representative example in this context is a recent report on a hydrogel-protected DNA aptamer-based sensor using agarose hydrogel to prevent enzymatic degradation of the analyte-recognizing aptamer and biocomponent interferent adsorption [79].

13   Chemical sensors

The possibility to load the PEG matrix of the PHFs and PHNs with NPs allows the fabrication of chemical sensors on the PHF/PHN basis, relying on the catalytic properties of the embedded NPs. A representative example in this context is a sensor for hydrogen peroxide (H_2O_2) [80], which is an important compound both in the industry and medicine, serving, in particular, as a marker for a variety of diseases, including cancer [81–86]. Sensing of H_2O_2 can be generally performed by both enzyme-based detection, with enzymes that are capable of catalyzing its decomposition [87–90], and by use of noble metal NPs, relying on their electrocatalytic properties concerning hydrogen peroxide [91–94].

On this basis, we have loaded PHFs (130 nm) with AuNPs (15 nm) within the one-pot preparation procedure and used electrochemical tools for the detection of H_2O_2 [80]. The PHFs were prepared on the primary, SiO_2 passivated Si(100) substrates and transferred from them, as the free-standing PHNs, to the working electrode of the electrochemical cell. The CV curves for the reference, pristine PHN and the composite PEG-AuNP film, acquired in the presence of H_2O_2, show a distinct signature of the electrocatalytic reaction in the latter case, with a pronounced reduction peak at ca. –0.15 eV (Fig. 15(a)). The respective reaction is schematically illustrated in Fig. 15(b), in which the amperometric response of the composite PEG-AuNP film to increase H_2O_2 concentration is presented. The respective current values are plotted in Fig. 15(c) vs. the H_2O_2 concentration, showing a nearly linear dependence on the latter parameter. According to these data, the sensitivity, detection limit, and operation range of the composite PEG-AuNP sensors were estimated at ~ 3.4 × 10² µA/(mM·cm²), 0.17 µM of H_2O_2, and 20 µM–3.5 mM of H_2O_2, respectively, which are well comparable with the best values for other types of H_2O_2 sensors reported recently in Refs. [92–97]. Finally, the selectivity of the composite PEG-AuNPs sensor was verified by an anti-interference test, viz. its exposure to a variety of potential interfering compounds and biomolecules, frequently found in biological samples, such as ascorbic acid (L-AA), biotin, and fibrinogen from human plasma. These compounds were successively added to the electrolyte, resulting in no noticeable current response at the given, preselected potential (Fig. 15(d)). In contrast, the addition of the same amount of H_2O_2 before and after the anti-interference tests
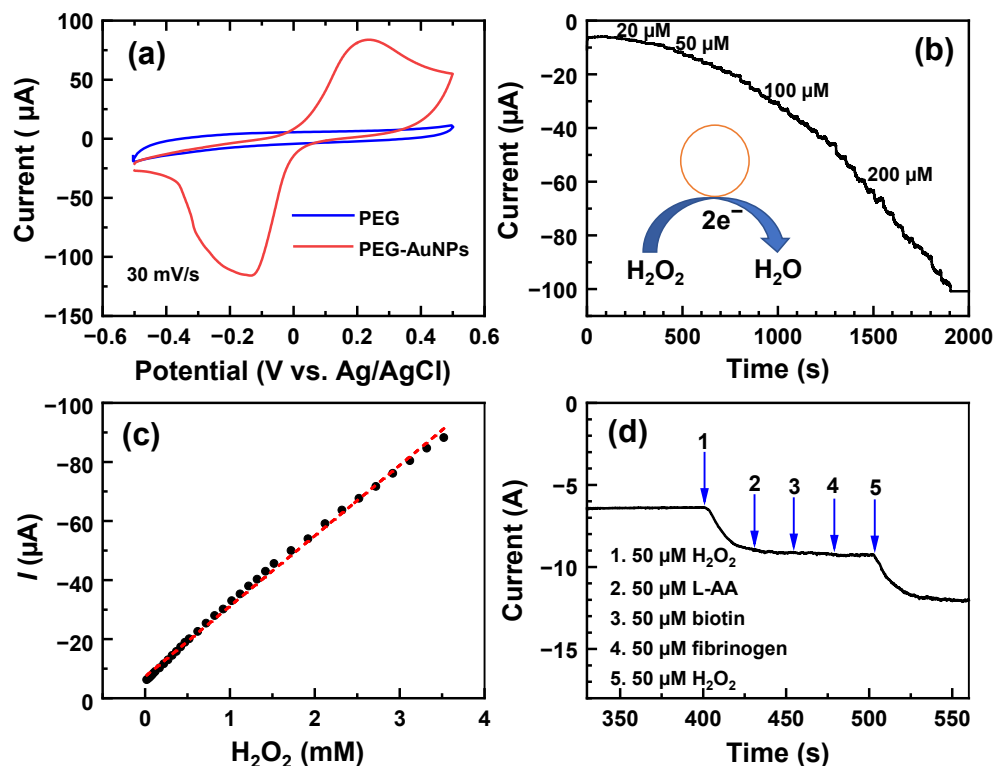
Figure 15 (a) CV curves for the reference, pristine PHN and the composite PEG-AuNP film measured in phosphate buffer solution at the presence of 2 mM H_2O_2. (b) Amperometric response of the composite PEG-AuNP film to increased H_2O_2 concentration upon successive, stepwise addition of different amounts of H_2O_2 to 50 mL of PBS buffer. The AuNP-catalyzed reaction is schematically illustrated. (c) Current response to the H_2O_2 concentration (black-filled circles), along with a linear fit to the experimental data (red dashed line). (d) Amperometric response of the composite PEG-AuNP film to the stepwise injection of H_2O_2 and potentially interfering substances into 50 mL of PBS. For the data presented in (b) and (d), the potential was set to –0.2 V. Reproduced with permission from Ref. [80], © Zhao, Z. Y. et al. 2023.

resulted, as expected, in a pronounced increase of the recorded current (Fig. 15(d)), proving the readability and active character of the sensor.

14   Conclusions

In summary, this review article is devoted to the fabrication, properties, and applications of PHFs and PHNs formed from the amino- and epoxy-decorated four-arm STAR-PEG precursors. The primary PHFs can be readily prepared on solid supports by a combination of spin-coating and thermally-promoted crosslinking reaction. They represent porous PEG films, with distinct hydrogel and bioinert properties. The thickness and porosity of these films can be flexibly adjusted in a broad range, viz. 5–280 nm for the thickness and 7–70 nm for the mesh size of the PEG matrix, by setting the concentration of the precursors in the primary solution and the choice of their molecular weight, respectively. The PHFs can be easily separated from the primary substrate as free-standing PHNs, which can be transferred to a secondary substrate or a supporting mesh. The PHNs retain all the favorite properties of the parent PHFs, exhibiting in addition exceptional elasticity and reversable deformation ability.

The adjustability and favorable properties of the PHFs and PHNs make them a versatile platform for hybrid materials, nanofabrication, lithography, and sensor applications. Representative examples in this context are provided, including bioinertness, hydrogel properties, morphology, and NP patterning as well as temperature, humidity, and biosensors. It is, however, reasonable to assume that the applications of the PHFs and PHNs are not only limited to these examples but can be extended to other tasks, such as delivery and controlled release of drugs, tissue engineering, biofouling protection, stimuli-responsive systems, terahertz-to-infrared converters for imaging the human skin cancer, etc. [4, 18, 19, 98].

References

[1] Jeon, S. I.; Lee, J. H.; Andrade, J. D.; De Gennes, P. G. Protein-

surface interactions in the presence of polyethylene oxide: I. *Simplified theory*. *J. Colloid Interface Sci.* **1991**, *142*, 149–158.

[2] Harris, J. M. *Poly(Ethylene Glycol) Chemistry: Biotechnical and Biomedical Applications*; Springer: New York, 1992.

[3] Rosenhahn, A.; Schilp, S.; Kreuzer, H. J.; Grunze, M. The role of "inert" surface chemistry in marine biofouling prevention. *Phys. Chem. Chem. Phys.* **2010**, *12*, 4275–4286.

[4] Zhao, X. B.; Si, J. X.; Huang, D. S.; Li, K.; Xin, Y.; Sui, M. Application of star poly(ethylene glycol) derivatives in drug delivery and controlled release. *J. Control. Release* **2020**, *323*, 565–577.

[5] Christophis, C.; Grunze, M.; Rosenhahn, A. Quantification of the adhesion strength of fibroblastcells on ethylene glycol terminated self-assembled monolayers by a microfluidic shear force assay. *Phys. Chem. Chem. Phys.* **2010**, *12*, 4498–4504.

[6] Shen, M. C.; Martinson, L.; Wagner, M. S.; Castner, D. G.; Ratner, B. D.; Horbett, T. A. PEO-like plasma polymerized tetraglyme surface interactions with leukocytes and proteins: *In vitro* and *in vivo* studies. *J. Biomater. Sci. Polym. Ed.* **2002**, *13*, 367–390.

[7] Prime, K. L.; Whitesides, G. M. Adsorption of proteins onto surfaces containing end-attached oligo(ethylene oxide): A model system using self-assembled monolayers. *J. Am. Chem. Soc.* **1993**, *115*, 10714–10721.

[8] Herrwerth, S.; Eck, W.; Reinhardt, S.; Grunze, M. Factors that determine the protein resistance of oligoether self-assembled monolayers-internal hydrophilicity, terminal hydrophilicity, and lateral packing density. *J. Am. Chem. Soc.* **2003**, *125*, 9359–9366.

[9] Kim, S.; Gim, T.; Jeong, Y.; Ryu, J. H.; Kang, S. M. Facile construction of robust multilayered PEG films on polydopamine-coated solid substrates for marine antifouling applications. *ACS Appl. Mater. Interfaces* **2018**, *10*, 7626–7631.

[10] Cambria, E.; Renggli, K.; Ahrens, C. C.; Cook, C. D.; Kroll, C.; Krueger, A. T.; Imperiali, B.; Griffith, L. G. Covalent modification of synthetic hydrogels with bioactive proteins via sortase-mediated ligation. *Biomacromolecules* **2015**, *16*, 2316–2326.

[11] Hammer, J. A.; Ruta, A.; Therien, A. M.; West, J. L. Cell-compatible, site-specific covalent modification of hydrogel scaffolds enables user-defined control over cell-material interactions. *Biomacromolecules* **2019**, *20*, 2486–2493.

[12] Larsson, A.; Ekblad, T.; Andersson, O.; Liedberg, B. Photografted poly(ethylene glycol) matrix for affinity interaction studies. *Biomacromolecules* **2007**, *8*, 287–295.

[13] Chen, R. T.; Marchesan, S.; Evans, R. A.; Styan, K. E.; Such, G. K.; Postma, A.; McLean, K. M.; Muir, B. W.; Caruso, F. Photoinitiated alkyne-azide click and radical cross-linking reactions for the patterning of PEG hydrogels. *Biomacromolecules* **2012**, *13*, 889–895.

[14] Cėpla, V.; Rakickas, T.; Stankevičienė, G.; Mazėtytė-Godienė, A.; Baradokė, A.; Ruželė, Ž.; Valiokas, R. Photografting and patterning of poly(ethylene glycol) methacrylate hydrogel on glass for biochip applications. *ACS Appl. Mater. Interfaces* **2020**, *12*, 32233–32246.

[15] Groll, J.; Amirgoulova, E. V.; Ameringer, T.; Heyes, C. D.; Röcker, C.; Nienhaus, G. U.; Möller, M. Biofunctionalized, Ultrathin coatings of cross-linked star-shaped poly(ethylene oxide) allow reversible folding of immobilized proteins. *J. Am. Chem. Soc.* **2004**, *126*, 4234–4239.

[16] Groll, J.; Ameringer, T.; Spatz, J. P.; Moeller, M. Ultrathin coatings from isocyanate-terminated star PEG prepolymers: Layer formation and characterization. *Langmuir* **2005**, *21*, 1991–1999.

[17] Gasteier, P.; Reska, A.; Schulte, P.; Salber, J.; Offenhäusser, A.; Moeller, M.; Groll, J. Surface grafting of PEO-based star-shaped molecules for bioanalytical and biomedical applications. *Macromol. Biosci.* **2007**, *7*, 1010–1023.

[18] Tan, H. P.; DeFail, A. J.; Rubin, J. P.; Chu, C. R.; Marra, K. G. Novel multiarm PEG-based hydrogels for tissue engineering. *J. Biomed. Mater. Res. A* **2010**, *92A*, 979–987.

[19] Zhu, J. M. Bioactive modification of poly(ethylene glycol) hydrogels for tissue engineering. *Biomaterials* **2010**, *31*, 4639–4656.

[20] Jeong, J. H.; Hong, S. W.; Hong, S.; Yook, S.; Jung, Y.; Park, J. B.; Khue, C. D.; Im, B. H.; Seo, J.; Lee, H. et al. Surface camouflage of pancreatic islets using 6-arm-PEG-catechol in combined therapy with tacrolimus and anti-CD154 monoclonal antibody for xenotransplantation. *Biomaterials* **2011**, *32*, 7961–7970.

[21] Teramura, Y.; Oommen, O. P.; Olerud, J.; Hilborn, J.; Nilsson, B. Microencapsulation of cells, including islets, within stable ultra-thin membranes of maleimide-conjugated PEG-lipid with multifunctional crosslinkers. *Biomaterials* **2013**, *34*, 2683–2693.

[22] Ding, M.; Jing, L.; Yang, H.; Machnicki, C. E.; Fu, X.; Li, K.; Wong, I. Y.; Chen, P. Y. Multifunctional soft machines based on stimuli-responsive hydrogels: From freestanding hydrogels to smart integrated systems. *Mater. Today Adv.* **2020**, *8*, 100088.

[23] Dong, Y. X.; Ramey-Ward, A. N.; Salaita, K. Programmable mechanically active hydrogel-based materials. *Adv. Mater.* **2021**, *33*, 2006600.

[24] El Sayed, M. M. Production of polymer hydrogel composites and their applications. *J. Polym. Environ.* **2023**, *31*, 2855–2879.

[25] Meyerbröker, N.; Kriesche, T.; Zharnikov, M. Novel ultrathin poly(ethylene glycol) films as flexible platform for biological applications and plasmonics. *ACS Appl. Mater. Interfaces* **2013**, *5*, 2641–2649.

[26] Zhao, Z. Y.; Das, S.; Zharnikov, M. Tuning the properties of poly(ethylene glycol) films and membranes by the molecular weight of the precursors. *ACS Appl. Polym. Mater.* **2022**, *4*, 645–653.

[27] Khan, M.; Schuster, S.; Zharnikov, M. Chemical derivatization and biofunctionalization of hydrogel nanomembranes for potential biomedical and biosensor applications. *Phys. Chem. Chem. Phys.* **2016**, *18*, 12035–12042.

[28] Zhao, Z. Y.; Zharnikov, M. Elastic properties of poly(ethylene glycol) nanomembranes and respective implications. *Membranes* **2022**, *12*, 509.

[29] Zhao, Z. Y.; Das, S.; Zharnikov, M. Rational design of porous poly(ethylene glycol) films as a matrix for ssDNA immobilization and hybridization. *Bioengineering* **2022**, *9*, 414.

[30] Zhao, Z. Y.; Zharnikov, M. Exploiting epoxy-rich poly(ethylene glycol) films for highly selective ssDNA sensing via electrochemical impedance spectroscopy. *Phys. Chem. Chem. Phys.* **2023**, *25*, 26538–26548.

[31] Meyerbröker, N.; Li, Z. A.; Eck, W.; Zharnikov, M. Biocompatible nanomembranes based on PEGylation of cross-linked self-assembled monolayers. *Chem. Mater.* **2012**, *24*, 2965–2972.

[32] Turchanin, A.; Gölzhäuser, A. Carbon nanomembranes. *Adv. Mater.* **2016**, *28*, 6075–6103.

[33] Scherr, J.; Parey, K.; Klusch, N.; Murphy, B. J.; Balser, S.; Neuhaus, A.; Zickermann, V.; Kühlbrandt, W.; Terfort, A.; Rhinow, D. Self-perforated hydrogel nanomembranes facilitate structural analysis of proteins by electron cryo-microscopy. *ACS Nano* **2017**, *11*, 6467–6473.

[34] Rodríguez-San-Miguel, D.; Montoro, C.; Zamora, F. Covalent organic framework nanosheets: Preparation, properties and applications. *Chem. Soc. Rev.* **2020**, *49*, 2291–2302.

[35] Scherr, J.; Tang, Z. A.; Küllmer, M.; Balser, S.; Scholz, A. S.; Winter, A.; Parey, K.; Rittner, A.; Grininger, M.; Zickermann, V. et al. Smart molecular nanosheets for advanced preparation of biological samples in electron cryo-microscopy. *ACS Nano* **2020**, *14*, 9972–9978.

[36] Balser, S.; Zhao, Z. Y.; Zharnikov, M.; Terfort, A. Effect of the crosslinking agent on the biorepulsive and mechanical properties of polyglycerol membranes. *Colloids Surf. B: Biointerfaces* **2023**, *225*, 113271.

[37] Meyerbröker, N.; Zharnikov, M. Ultraflexible, freestanding nanomembranes based on poly(ethylene glycol). *Adv. Mater.* **2014**, *26*, 3328–3332.

[38] Burdinski, D.; Blees, M. H. Thiosulfate- and thiosulfonate-based etchants for the patterning of gold using microcontact printing. *Chem. Mater.* **2007**, *19*, 3933–3944.

[39] Green, T. A. Gold etching for microfabrication. *Gold Bull.* **2014**, *47*, 205–216.

[40] Wilson, N. R.; Pandey, P. A.; Beanland, R.; Young, R. J.; Kinloch, I. A.; Gong, L.; Liu, Z.; Suenaga, K.; Rourke, J. P.; York, S. J. et al. Graphene oxide: Structural analysis and application as a highly transparent support for electron microscopy. *ACS Nano* **2009**, *3*, 2547–2556.

[41] Small, M. K.; Vlassak, J. J.; Powell, S. F.; Daniels, B. J.; Nix, W. D. Accuracy and reliability of bulge test experiments. *MRS Online Proc. Lib.* **1993**, *308*, 159–164.

[42] Zamprogno, P.; Thoma, G.; Cencen, V.; Ferrari, D.; Putz, B.; Michler, J.; Fantner, G. E.; Guenat, O. T. Mechanical properties of soft biological membranes for organ-on-a-chip assessed by bulge test and AFM. *ACS Biomater. Sci. Eng.* **2021**, *7*, 2990–2997.

[43] Khan, M.; Schuster, S.; Zharnikov, M. Effect of humidity on electrical conductivity of pristine and nanoparticle-loaded hydrogel nanomembranes. *J. Phys. Chem. C* **2015**, *119*, 14427–14433.

[44] Zhao, Z. Y.; Das, S.; Zharnikov, M. Poly(ethylene glycol)-fullerene composite films and free-standing nanosheets for flexible electronic devices and sensors. *ACS Appl. Nano Mater.* **2023**, *6*, 2151–2161.

[45] Jehoulet, C.; Obeng, Y. S.; Kim, Y. T.; Zhou, F. M.; Bard, A. J. Electrochemistry and Langmuir trough studies of C_{60} and C_{70} films. *J. Am. Chem. Soc.* **1992**, *114*, 4237–4247.

[46] Bond, A. M.; Miao, W. J.; Raston, C. L. Identification of processes that occur after reduction and dissolution of C_{60} adhered to gold, glassy carbon, and platinum electrodes placed in acetonitrile (electrolyte) solution. *J. Phys. Chem. B* **2000**, *104*, 2320–2329.

[47] Meyerbröker, N.; Zharnikov, M. Modification and patterning of nanometer-thin poly(ethylene glycol) films by electron irradiation. *ACS Appl. Mater. Interfaces* **2013**, *5*, 5129–5138.

[48] Meyerbröker, N.; Zharnikov, M. Hydrogel nanomembranes as templates for patterned deposition of nanoparticles on arbitrary substrates. *ACS Appl. Mater. Interfaces* **2014**, *6*, 14729–14735.

[49] Zhao, Z. Y.; Yan, R.; Zharnikov, M. The effect of ultraviolet light on biorepulsive hydrogel poly(ethylene glycol) films. *ACS Appl. Polym. Mater.* **2021**, *3*, 3446–3454.

[50] Holland, W. R.; Hall, D. G. Frequency shifts of an electric-dipole resonance near a conducting surface. *Phys. Rev. Lett.* **1984**, *52*, 1041–1044.

[51] Leitner, A.; Zhao, Z. S.; Brunner, H.; Aussenegg, F. R.; Wokaun, A. Optical properties of a metal island film close to a smooth metal surface. *Appl. Opt.* **1993**, *32*, 102–110.

[52] Aussenegg, F. R.; Brunner, H.; Leitner, A.; Lobmaier, C.; Schalkhammer, T.; Pittner, F. The metal island coated swelling polymer over mirror system (MICSPOMS): A new principle for measuring ionic strength. *Sens. Actuators B: Chem.* **1995**, *29*, 204–209.

[53] Krishnakumar, T.; Jayaprakash, R.; Singh, V. N.; Mehta, B. R.; Phani, A. R. Synthesis and characterization of tin oxide nanoparticle for humidity sensor applications. *J. Nano Res.* **2008**, *4*, 91–101.

[54] Pissis, P.; Kyritsis, A. Electrical conductivity studies in hydrogels. *Solid State Ionics* **1997**, *97*, 105–113.

[55] Rittersma, Z. M. Recent achievements in miniaturised humidity sensors-a review of transduction techniques. *Sens. Actuators A: Phys.* **2002**, *96*, 196–210.

[56] Yeh, H. W.; Ai, H. W. Development and applications of bioluminescent and chemiluminescent reporters and biosensors. *Annu. Rev. Anal. Chem.* **2019**, *12*, 129–150.

[57] Udugama, B.; Kadhiresan, P.; Kozlowski, H. N.; Malekjahani, A.; Osborne, M.; Li, V. Y. C.; Chen, H. M.; Mubareka, S.; Gubbay, J. B.; Chan, W. C. W. Diagnosing COVID-19: The disease and tools for detection. *ACS Nano* **2020**, *14*, 3822–3835.

[58] Quijano-Rubio, A.; Yeh, H. W.; Park, J.; Lee, H.; Langan, R. A.; Boyken, S. E.; Lajoie, M. J.; Cao, L. X.; Chow, C. M.; Miranda, M. C. et al. De novo design of modular and tunable protein biosensors. *Nature* **2021**, *591*, 482–487.

[59] Ratner, B. D.; Castner, D. G. Electron spectroscopy for chemical analysis. In *Surface Analysis-The Principal Techniques*. Vickerman, J. C., Ed.; John Wiley & Sons: Chichester, UK, 1997; pp 43–98.

[60] Rao, A. N.; Grainger, D. W. Biophysical properties of nucleic acids at surfaces relevant to microarray performance. *Biomater. Sci.* **2014**, *2*, 436–471.

[61] Zhang, X. N.; Hu, H. M. DNA Molecules site-specific immobilization and their applications. *Cent. Eur. J. Chem.* **2014**, *12*, 977–993.

[62] Du, Y.; Dong, S. J. Nucleic acid biosensors: Recent advances and perspectives. *Anal. Chem.* **2017**, *89*, 189–215.

[63] Babaei, A.; Pouremamali, A.; Rafiee, N.; Sohrabi, H.; Mokhtarzadeh, A.; de la Guardia, M. Genosensors as an alternative diagnostic sensing approaches for specific detection of virus species: A review of common techniques and outcomes. *TrAC Trends Anal. Chem.* **2022**, *155*, 116686.

[64] Zhao, J.; Di, Z. H.; Li, L. L. Spatiotemporally selective molecular imaging via upconversion luminescence-controlled, DNA-based biosensor technology. *Angew. Chem., Int. Ed.* **2022**, *61*, e202204277.

[65] Petrovykh, D. Y.; Kimura-Suda, H.; Whitman, L. J.; Tarlov, M. J. Quantitative analysis and characterization of DNA immobilized on gold. *J. Am. Chem. Soc.* **2003**, *125*, 5219–5226.

[66] Petrovykh, D. Y.; Pérez-Dieste, V.; Opdahl, A.; Kimura-Suda, H.; Sullivan, J. M.; Tarlov, M. J.; Himpsel, F. J.; Whitman, L. J. Nucleobase orientation and ordering in films of single-stranded DNA on gold. *J. Am. Chem. Soc.* **2006**, *128*, 2–3.

[67] Opdahl, A.; Petrovykh, D. Y.; Kimura-Suda, H.; Tarlov, M. J.; Whitman, L. J. Independent control of grafting density and conformation of single-stranded DNA brushes. *Proc. Natl. Acad. Sci. USA* **2007**, *104*, 9–14.

[68] Schreiner, S. M.; Hatch, A. L.; Shudy, D. F.; Howard, D. R.; Howell, C.; Zhao, J. L.; Koelsch, P.; Zharnikov, M.; Petrovykh, D. Y.; Opdahl, A. Impact of DNA-surface interactions on the stability of DNA hybrids. *Anal. Chem.* **2011**, *83*, 4288–4295.

[69] Howell, C.; Jeyachandran, Y. L.; Koelsch, P.; Zharnikov, M. Orientation and ordering in sequence- and length-mismatched surface-bound DNA hybrids. *J. Phys. Chem. C* **2012**, *116*, 11133–11140.

[70] Stuparu, M. C.; Khan, A. Thiol-epoxy "click" chemistry: Application in preparation and postpolymerization modification of polymers. *J. Polym. Sci. Part A: Polym. Chem.* **2016**, *54*, 3057–3070.

[71] Yang, B. Q.; Gordiyenko, K.; Schäfer, A.; Dadfar, S. M. M.; Yang, W. W.; Riehemann, K.; Kumar, R.; Niemeyer, C. M.; Hirtz, M. Fluorescence imaging study of film coating structure and composition effects on DNA hybridization. *Adv. NanoBiomed Res.* **2023**, *3*, 2200133.

[72] Ballav, N.; Koelsch, P.; Zharnikov, M. Orientation and ordering in monomolecular films of sulfur-modified homo-oligonucleotides on gold. *J. Phys. Chem. C* **2009**, *113*, 18312–18320.

[73] Han, H. W.; Sabani, N. B.; Nobusawa, K.; Takei, F.; Nakatani, K.; Yamashita, I. On-demand ligand-base DNA sensor with electrochemical impedance spectroscopy. *Anal. Chem.* **2023**, *95*, 9729–9733.

[74] Kivlehan, F.; Paolucci, M.; Brennan, D.; Ragoussis, I.; Galvin, P. Three-dimensional hydrogel structures as optical sensor arrays, for the detection of specific DNA sequences. *Anal. Biochem.* **2012**, *421*, 1–8.

[75] Jamaluddin, R. Z. A. R.; Tan, L. L.; Chong, K. F.; Heng, L. Y. An electrochemical DNA biosensor fabricated from graphene decorated with graphitic nanospheres. *Nanotechnology* **2020**, *31*, 485501.

[76] Raymundo-Pereira, P. A.; de Oliveira Pedro, R.; Carr, O.; Melendez, M. E.; Gobbi, A. L.; de Oliveira Piazzetta, M. H.; Carvalho, A. L.; Reis, R. M.; Miranda, P. B.; Oliveira, O. N. Jr. Influence of the molecular orientation and ionization of self-assembled monolayers in biosensors: Application to genosensors of prostate cancer antigen 3. *J. Phys. Chem. C* **2021**, *125*, 498–506.

[77] Lee, C. Y.; Nguyen, P. C. T.; Grainger, D. W.; Gamble, L. J.; Castner, D. G. Structure and DNA hybridization properties of mixed nucleic acid/maleimide-ethylene glycol monolayers. *Anal. Chem.* **2007**, *79*, 4390–4400.

[78] Howell, C.; Zhao, J. L.; Koelsch, P.; Zharnikov, M. Hybridization in ssDNA films-a multi-technique spectroscopy study. *Phys. Chem. Chem. Phys.* **2011**, *13*, 15512–15522.

[79] Li, S. G.; Dai, J.; Zhu, M.; Arroyo-Currás, N.; Li, H. X.; Wang, Y. Y.; Wang, Q.; Lou, X. D.; Kippin, T. E.; Wang, S. X. et al. Implantable hydrogel-protective DNA aptamer-based sensor supports accurate, continuous electrochemical analysis of drugs at multiple sites in living rats. *ACS Nano* **2023**, *17*, 18525–18538.

[80] Zhao, Z. Y.; Zharnikov, M. Gold nanoparticle-loaded porous poly(ethylene glycol) nanosheets for electrochemical detection of H_2O_2. *Nanomaterials* **2023**, *13*, 3137.

[81] Veal, E. A.; Day, A. M.; Morgan, B. A. Hydrogen peroxide sensing and signaling. *Mol. Cell* **2007**, *26*, 1–14.

[82] Maji, S. K.; Sreejith, S.; Mandal, A. K.; Ma, X.; Zhao, Y. L. Immobilizing gold nanoparticles in mesoporous silica covered reduced graphene oxide: A hybrid material for cancer cell detection through hydrogen peroxide sensing. *ACS Appl. Mater. Interfaces* **2014**, *6*, 13648–13656.

[83] Dong, Z. L.; Yang, Z. J.; Hao, Y.; Feng, L. Z. Fabrication of H_2O_2-driven nanoreactors for innovative cancer treatments. *Nanoscale* **2019**, *11*, 16164–16186.

[84] Yang, B. W.; Chen, Y.; Shi, J. L. Reactive oxygen species (ROS)-based nanomedicine. *Chem. Rev.* **2019**, *119*, 4881–4985.

[85] An, H. J.; Guo, C. H.; Li, D. D.; Liu, R. F.; Xu, X. Q.; Guo, J. W.; Ding, J.; Li, J. J.; Chen, W.; Zhang, J. X. Hydrogen peroxide-activatable nanoparticles for luminescence imaging and *in situ* triggerable photodynamic therapy of cancer. *ACS Appl. Mater. Interfaces* **2020**, *12*, 17230–17243.

[86] Ahmad, T.; Iqbal, A.; Halim, S. A.; Uddin, J.; Khan, A.; El Deeb, S.; Al-Harrasi, A. Recent advances in electrochemical sensing of hydrogen peroxide (H_2O_2) released from cancer cells. *Nanomaterials* **2022**, *12*, 1475.

[87] Feng, J. J.; Zhao, G.; Xu, J. J.; Chen, H. Y. Direct electrochemistry and electrocatalysis of heme proteins immobilized on gold nanoparticles stabilized by chitosan. *Anal. Biochem.* **2005**, *342*, 280–286.

[88] Chen, L.; Lu, G. X. Direct electrochemistry and electrocatalysis of hybrid film assembled by polyelectrolyte-surfactant polymer, carbon nanotubes and hemoglobin. *J. Electroanal. Chem.* **2006**, *597*, 51–59.

[89] Gao, F. X.; Yuan, R.; Chai, Y. Q.; Chen, S. H.; Cao, S. R.; Tang, M. Y. Amperometric hydrogen peroxide biosensor based on the immobilization of HRP on nano-Au/Thi/poly (p-aminobenzene sulfonic acid)-modified glassy carbon electrode. *J. Biochem. Biophys. Methods* **2007**, *70*, 407–413.

[90] Yagati, A. K.; Lee, T.; Min, J. H.; Choi, J. W. Electrochemical performance of gold nanoparticle-cytochrome c hybrid interface for H_2O_2 detection. *Colloids Surf. B: Biointerfaces* **2012**, *92*, 161–167.

[91] Bai, Z. H.; Li, G. Y.; Liang, J. T.; Su, J.; Zhang, Y.; Chen, H. Z.; Huang, Y.; Sui, W.; Zhao, Y. X. Non-enzymatic electrochemical biosensor based on Pt NPs/RGO-CS-Fc nano-hybrids for the detection of hydrogen peroxide in living cells. *Biosens. Bioelectron.* **2016**, *82*, 185–194.

[92] Chen, S. Y.; Xie, Y. X.; Guo, X. J.; Sun, D. P. Self-supporting electrochemical sensors for monitoring of cell-released H_2O_2 based on metal nanoparticle/MOF nanozymes. *Microchem. J.* **2022**, *181*, 107715.

[93] Zhang, Y. W.; Chen, Q.; Guo, A.; Wang, X. L.; Wang, Y.; Long, Y.; Fan, G. Y. Carbon-nanosheet-driven spontaneous deposition of Au nanoparticles for efficient electrochemical utilizations toward H_2O_2 generation and detection. *Chem. Eng. J.* **2022**, *445*, 136586.

[94] Yuan, J.; Chen, Q.; Xiao, Y. L.; Li, D. D.; Jiang, X. M.; Wu, P. Cobalt-based layered double hydroxide nanosheet-supported AuNPs for high performance electrochemical H_2O_2 detection. *Appl. Surf. Sci.* **2023**, *630*, 157463.

[95] Gholami, M.; Koivisto, B. A flexible and highly selective non-enzymatic H_2O_2 sensor based on silver nanoparticles embedded into Nafion. *Appl. Surf. Sci.* **2019**, *467–468*, 112–118.

[96] Xia, C.; He, W.; Yang, X. F.; Gao, P. F.; Zhen, S. J.; Li, Y. F.; Huang, C. Z. Plasmonic hot-electron-painted Au@Pt nanoparticles as efficient electrocatalysts for detection of H_2O_2. *Anal. Chem.* **2022**, *94*, 13440–13446.

[97] Giaretta, J. E.; Duan, H. W.; Oveissi, F.; Farajikhah, S.; Dehghani, F.; Naficy, S. Flexible sensors for hydrogen peroxide detection: A critical review. *ACS Appl. Mater. Interfaces* **2022**, *14*, 20491–20505.

[98] Moldosanov, K.; Bykov, A.; Kairyev, N.; Khodzitsky, M.; Kropotov, G.; Lelevkin, V.; Meglinski, I.; Postnikov, A.; Shakhmin, A. Terahertz-to-infrared converters for imaging the human skin cancer: Challenges and feasibility. *J. Med. Imaging* **2023**, *10*, 023501.